analytical chemistry

pubs.acs.org/ac Article

# Label-Free Autofluorescence-Detected Mid-Infrared Photothermal Microscopy of Pharmaceutical Materials

Aleksandr Razumtcev,[‖] Minghe Li,[‖] Jiayue Rong, Chu C. Teng, Christian Pfluegl, Lynne S. Taylor, and Garth J. Simpson*

Cite This: *Anal. Chem.* 2022, 94, 6512−6520 Read Online

ACCESS | Metrics & More | Article Recommendations | Supporting Information

**ABSTRACT:** Label-free autofluorescence-detected photothermal mid-IR (AF-PTIR) microscopy is demonstrated experimentally and applied to test the distribution of active pharmaceutical ingredients (APIs) in a mixture containing representative pharmaceutical excipients. Two-photon excited UV-fluorescence (TPE-UVF) supports autofluorescence of native aromatic moieties using visible-light optics. Thermal modulation of the fluorescence quantum yield serves to report on infrared absorption, enabling infrared spectroscopy in the fingerprint region with a spatial resolution dictated by fluorescence. AF-PTIR provides high selectivity and sensitivity in image contrast for aromatic APIs, complementing broadly applicable optical photothermal IR (O-PTIR) microscopy based on photothermal modulation of refractive index/scattering. Mapping the API distribution is critical in designing processes for powdered dosage form manufacturing, with high spatial variance potentially producing variability in both delivered dosage and product efficacy. The ubiquity of aromatic moieties within API candidates suggests the viability of AF-PTIR in combination with O-PTIR to improve the confidence of chemical classification in spatially heterogeneous dosage forms.

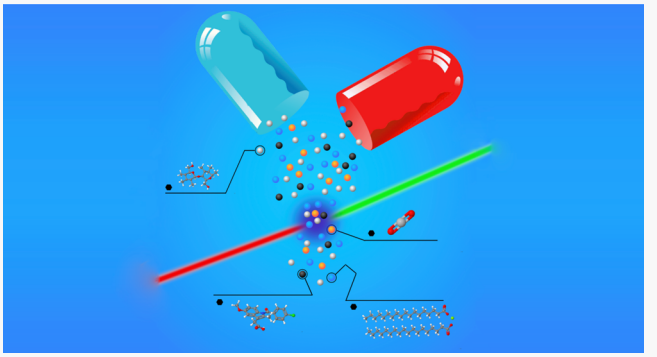



## INTRODUCTION

Quantifying the spatial distribution of an active pharmaceutical ingredient (API) within the final dosage forms is an important step of drug product quality control. One of the main reasons for product recall of solid dosage forms is lack of content uniformity.[1] The particle size and mixture ratio are among the crucial factors considered during the development of solid dosage forms, as they directly impact the bioavailability, dissolution rates and dosage unit content uniformity.[2] Hence, identifying potential inhomogeneous distribution of the API particles is important for ensuring reproducible bioavailability within final dosage forms.[3] Analytical tools capable of rapidly and accurately informing on the quantitative distribution of solid-state composition within final dosage forms are critical for control uniformity in dosage form manufacturing.

Several analytical techniques capable of mapping the chemical composition at the micron scale have been proposed for addressing this need. Matrix-assisted laser desorption/ionization mass spectrometry (MALDI MS or MALDI-TOF MS) was shown to achieve 1.4 $\mu$m spatial resolution with high chemical specificity and low limits of detection.[4−6] However, the MALDI-MS sometimes leads to sample damage, suffers from low throughput, and requires an additional step in sample preparation.[7] Furthermore, finding a suitable matrix also presents a challenge in case of pharmaceutical substances.[8]

Many recently introduced microspectroscopy techniques rely on IR spectroscopy for chemical identification. Direct infrared microscopy in the fingerprint region utilizes far-field apertures to maximize the amount of IR radiation delivered to the focal plane for improved image quality.[9] However, due to the long wavelength of light, direct IR imaging in the fingerprint region is diffraction-limited at spatial resolution of 5−10 $\mu$m, which might be insufficient for many applications.[10−12]

Raman spectroscopy has the potential to address the resolution limits of direct IR absorption/scattering microscopy, with several different implementations suggested previously.[13] Conventional Raman spectroscopy is complementary to IR-based methods in accessing spectral information, and it routinely achieves submicron resolution.[14] However, spontaneous Raman measurements usually require long integration times due to weak Raman cross sections of most analytes. More recently, coherent Raman spectroscopy, including stimulated Raman scattering (SRS) and coherent anti-Stokes

Received: December 20, 2021
Accepted: April 13, 2022
Published: April 21, 2022




https://doi.org/10.1021/acs.analchem.1c05504
*Anal. Chem.* 2022, 94, 6512−6520

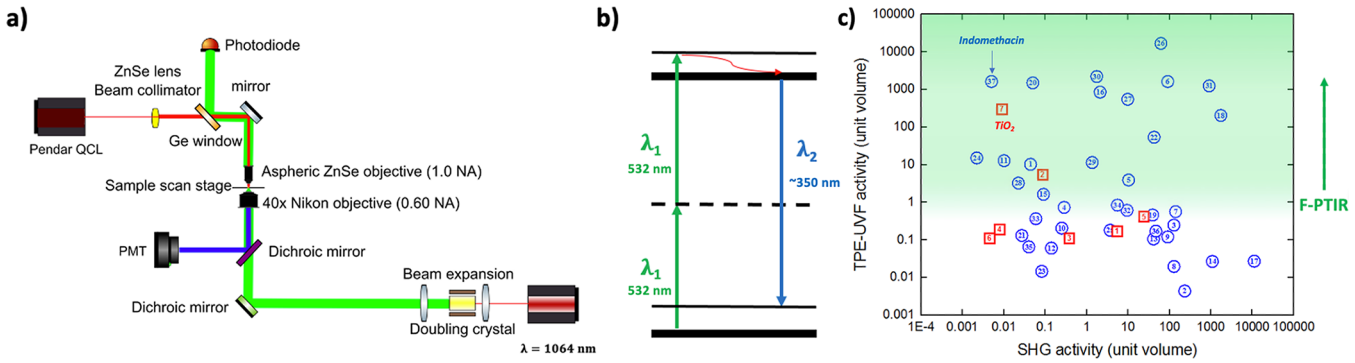


**Figure 1.** (a) AF-PTIR microscope instrumentation. The beam path for the 532 nm excitation laser is shown in green. The QCL beam path is shown in red, and the UV-fluorescence detection scheme is shown in blue. (b) TPE-UVF energy diagram. (c) TPE-UVF and SHG activities of selected APIs and excipients (see the Supporting Information for the legend). The green region highlights the materials that can potentially studied by AF-PTIR.

Raman spectroscopy (CARS), have been shown to perform high speed, high resolution chemical microscopy.[15] However, these methods require expensive instrumentation and are not cost-efficient for industrial use yet.[16] Furthermore, relative to IR absorption, the shorter visible wavelengths associated with both spontaneous and stimulated Raman increase optical scatter and restrict analysis to a fairly narrow depth immediately adjacent to the interface. To overcome the inherent low resolution of IR microscopy, photothermal mid-IR techniques were introduced.

Photothermal atomic force infrared microscopy (AFM-IR) is a scanning probe technique combining nanoscale spatial resolution and the rich chemical information gained with infrared spectroscopy.[17,18] The key concept behind AFM-IR is detecting the sample thermal expansion resulting from local heating caused by the absorption of infrared radiation. However, the AFM-IR applications are constrained to just those species immediately adjacent to a scanning probe tip and require relatively long acquisition times. Optically detected photothermal mid-IR (O-PTIR) microscopy is capable of measuring vibrational absorption spectra by detecting subtle changes in refractive index caused by thermal expansion.[19−21] O-PTIR was demonstrated to reach subdiffraction spatial resolution when imaging polymeric beads.[22,23] Li et al. used O-PTIR microscopy to map the distribution of components within a drug tablet.[24] Despite these successes, O-PTIR faces numerous challenges. First, in many cases O-PTIR intensity is biased toward the particles that scatter incident light more efficiently, which might challenge quantitative spectral analysis. Furthermore, O-PTIR suffers from nontrivial point spread functions in transmission dark-field configuration.[25]

An alternative detection scheme based on measuring temperature-induced changes in fluorescence quantum efficiency has been recently independently developed by Simpson and co-workers[26] and Cheng and co-workers.[27] Fluorescence-detected photothermal mid-IR (F-PTIR) microscopy was shown to achieve at least an order of magnitude signal-to-noise improvement over conventional O-PTIR and was applied for living cell imaging[27] and characterization of phase separated microdomains in pharmaceutical amorphous solid dispersions.[26] Notably, the use of fluorescence enabled analysis of vibrational spectroscopy immediately adjacent to fluorescent regions of interest (e.g., targeted by selective chemical labeling with fluorophores). This suppression of background interference from nonfluorescent regions can greatly improve sensitivity and selectivity. However, in some instances the addition of a fluorescent reporter also has the potential to limit the breadth of applications for F-PTIR microscopy and might introduce perturbations to the studied system.[28,29]

The ubiquitous presence of native autofluorescence in the UV region for most proteins and many active pharmaceutical ingredients raises the interesting possibility of integrating F-PTIR with autofluorescence for label-free analysis. The use of UV absorption (and to a lesser extent, fluorescence) is well established for selective detection of proteins, finding widespread use in chromatography.[30,31] Similarly, aromatic amino acids are ubiquitous within therapeutic proteins.[32] For API analysis, previous studies by Toth et al. have reported two-photon excited UV-autofluorescence (TPE-UVF) from numerous active pharmaceutical ingredients.[33,34] Unlike direct UV-b absorption, multiphoton excitation with ultrafast visible light sources offers several practical advantages, including compatibility with conventional glass optics and intrinsic optical sectioning within turbid media, such as powders and compacts.[35]

Fluorescence-based methods have been explored previously for pharmaceutical materials analysis, leveraging the ubiquitous incorporation of aromatic moieties within many small molecule APIs. Chen et al. has developed a UV-fluorescence based instrument for determination of amiloride (AMI) in pharmaceutical tablets and human serum.[36] Toth and co-workers compared UV-SHG with TPE-UVF for API detection, demonstrating reasonably high selectivity for APIs by TPE-UVF.[33] However, use of fluorescence as a stand-alone method can be problematic from a measurement science perspective. Most notably, many common excipients exhibit native TPE-UVF signals (e.g., $TiO_2$ and HPMC), reducing the selectivity for the API. Furthermore, minute quantities of trace impurities following synthesis may potentially contribute to background UV autofluorescence in poorly controlled manners. Other unexpected sources of TPE-UVF background may also potentially interfere with selective detection of the API, such as surface defects,[37] amine-oxygen exciplex formation,[38] and proteinaceous airborne particulates.[39] Spectroscopically, emission spectra of these different fluorescence sources tend to be broad and highly overlapping in the UV, complicating reliable spectral decomposition. Short fluorescence lifetimes common in the UV region also tend to minimize the potential benefits of lifetime imaging. Consequently, there are advantages to utilizing spectral signals more directly dependent on molecular


https://doi.org/10.1021/acs.analchem.1c05504
Anal. Chem. 2022, 94, 6512−6520

and macromolecular structure, while still seeking to leverage the preferential contrast of intrinsic autofluorescence.

In this work, autofluorescence-detected photothermal infrared (AF-PTIR) spectroscopy is demonstrated experimentally and applied to recover the fingerprint region spectra of individual API (indomethacin) particles with high selectivity in powdered mixtures of common excipients. The AF-PTIR microscope system supports multimodal nonlinear microscopy combining mid-IR microspectroscopy with symmetry-specific second harmonic generation (SHG) imaging and two-photon excited UV-fluorescence microscopy (TPE-UVF). Multimodal imaging in combination with AF-PTIR enabled chemical classification of individual particulates within mixtures designed to be representative of the final dosage forms.

## EXPERIMENTAL METHODS

**AF-PTIR Microscope Setup.** A custom multimodal nonlinear microscope system was used for bright field, TPE-UVF, AF-PTIR, O-PTIR (all at 532 nm incident wavelength), and SHG (1064 nm incident light) imaging. The instrument utilized an ultrafast excitation beam counter-propagating with a mid-IR pump beam as shown in Figure 1a. The excitation beam was generated by a 50 MHz 1064 nm femtosecond laser (Fianium FemtoPower; 185 fs pulse duration at 1 W power), which was frequency-doubled to produce an ultrafast 532 nm beam for laser transmittance imaging and two-photon excitation (Figure 1b). The laser was focused on a sample by using a 40× 0.60 NA Nikon Plan Fluor ELWD objective. A mid-IR array of 32 independent quantum cascade lasers (QCL) covering the spectral range between 1054 and 1186 $cm^{-1}$ (Pendar Technologies) was used as an IR source. An aspheric ZnSe objective (Edmund Optics, 1.0 NA) was used to focus the pump beam to the sample plane. The QCL produced 300 ns pulses at 33 kHz repetition rate during a 500 $\mu$s "on" window, described in detail in prior work.[26] The duty cycle within the burst period was maintained at 1%. An 80 MHz function generator was used to externally trigger the QCL (Agilent).

Autofluorescence signal was collected with a photomultiplier tube (PMT, Hamamatsu H10721-210) in an epi-configuration. Following isolation using a 500 nm long-pass dichroic mirror (Edmund Optics), combination of a 532 nm notch filter (Semrock StopLine), a 506 nm short-pass filter (Edmund Optics), and a 532 nm short-pass filter (Semrock RazorEdge) was used to suppress the excitation light.

To collect the SHG signal, a visible blocking filter was installed after the doubling crystal to suppress the doubled frequency and pass the fundamental 1064 nm light. The polarization state of the attenuated beam was adjusted with a waveplate to suppress SHG within the doubling crystal. The SHG signal from the sample plane was collected with the same PMT used for UV-fluorescence measurements after replacing the dichroic mirror (570 nm long-pass) and PMT filter set (Thorlabs KG3 filter and Edmund Optics 530±15 nm bandpass filter).

For bright field imaging, the transmitted 532 nm incident light was collected with a photodiode (Thorlabs DET10A) as shown in Figure 1a.

**Signal Processing and Image Generation.** All images were generated by scanning the samples mounted on a piezoelectric stage (MadCityLabs Nano-BIO 300). For AF-PTIR imaging, the raw PMT readout was first electronically frequency filtered (ITHACO 4302 Dual 24 dB Octave) to retain the frequency components in a narrow window around the QCL modulation frequency, and the bandpass filtered signal was subsequently digitized using an AlazarTech ATS9462 waveform digitizer. The digitizer was externally clocked by the same function generator used to modulate the trigger signal for the QCL. In-house MATLAB software was used to average the signal over multiple QCL modulation periods on each pixel.

Digital lock-in amplification was performed by fitting the resulting waveforms to a sine function to recover amplitude and phase relative to the QCL trigger signal. The calculated amplitude on each pixel was used as the AF-PTIR signal intensity to construct the image. The total image acquisition time was 75 s for 50 × 50 pixels AF-PTIR images and 300 s for a higher-resolution 100 × 100 pixels images with a 30 ms pixel dwell time in both cases.

For two-photon excited UV-fluorescence, SHG, and bright field imaging, the preamplified detected signal was low-pass filtered with a 1.6 kHz cutoff frequency to remove high-frequency components and then digitized. The acquisition time was 20 s to produce 200 × 200 pixels images with a 500 $\mu$s pixel dwell time.

**O-PTIR Imaging.** Optically detected photothermal mid-IR microscopy was conducted on the AF-PTIR system in a backscattered configuration. The TPE-UVF dichroic mirror was replaced with a glass slide at 45° to reflect a fraction of the backscattered incident light. The TPE-UVF filter set in front of the PMT was replaced by a 530 nm bandpass filter (Chroma HQ530/30m). The data analysis procedure was analogous to the one used for AF-PTIR.

**FTIR Characterization.** FTIR spectra for all components were collected on a Thermo-Nicolet Nexus 470 FTIR spectrometer operating in a total internal reflectance configuration using a diamond substrate, with 1 $cm^{-1}$ spectral resolution.

**Mixture Preparation.** Pure indomethacin (Letco Medical USP, 685406), lactose monohydrate ($\alpha$-polymorph, compendial, impalpable grind), magnesium stearate (compendial, nonbovine), and titanium dioxide (325 mesh, 99% purity, Sigma-Aldrich) powders were used for individual components characterization and mixture preparation. Lactose monohydrate (MH) and indomethacin particles were filtered by size between 25 and 125 $\mu$m sieves and then physically mixed with other components in a 1:1:1:1 mass ratio to produce a tabletlike mixture. Powdered samples were prepared on mid-IR transparent amorphous calcium fluoride microscope slide substrates (UQG Optics)

**Powder X-ray Diffraction.** Powder X-ray diffraction (PXRD) patterns of indomethacin were acquired by using a Panalytical Empyrean powder X-ray diffractometer with Cu $K_\alpha$ irradiation at room temperature. The measurements were conducted using a reflection/transmission spinner. Rietveld refinement was conducted for fitting the experimental data.

## RESULTS AND DISCUSSION

**Label-Free AF-PTIR Spectroscopy of Pure Indomethacin.** Label-free AF-PTIR microscopy was applied to acquire a mid-IR absorption spectrum of indomethacin crystals. Indomethacin is a small-molecule anti-inflammatory drug containing aromatic conjugation in its structure and, therefore, has potential to exhibit substantial TPE-UVF activity. Consistent with these expectations, a strong TPE-UVF response was observed from indomethacin microcrystals


https://doi.org/10.1021/acs.analchem.1c05504
Anal. Chem. 2022, 94, 6512−6520

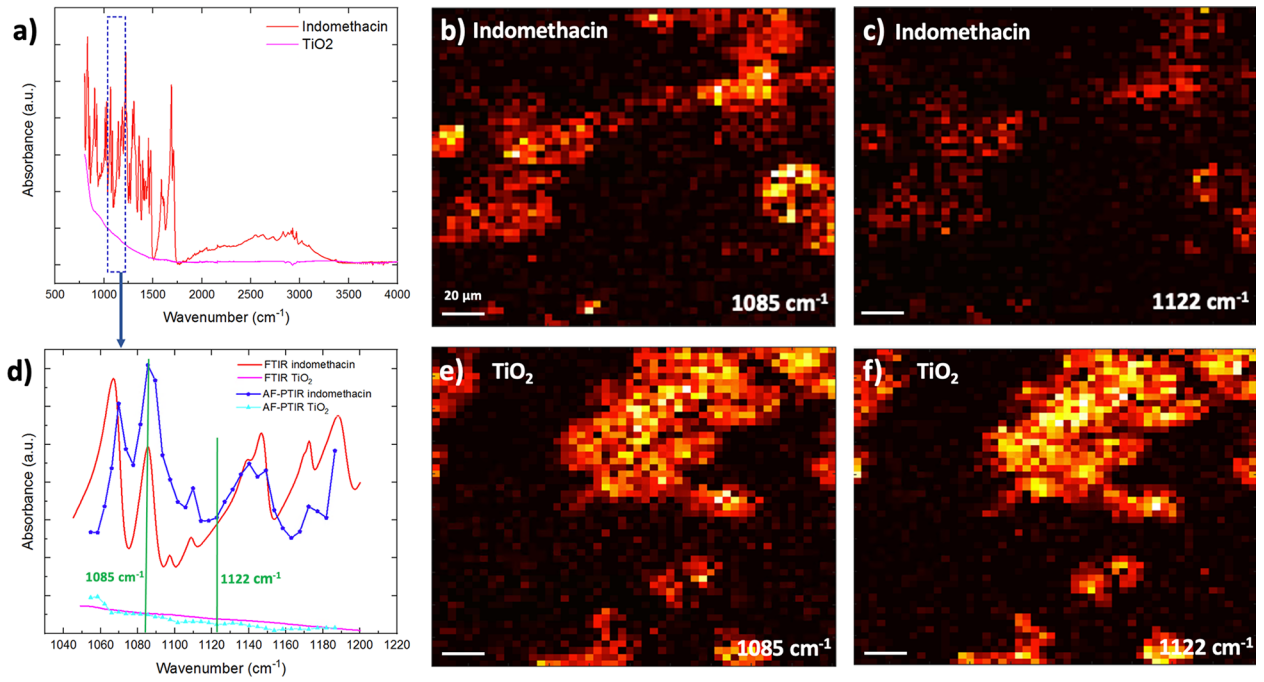


**Figure 2.** AF-PTIR spectroscopy of indomethacin and titanium dioxide. (a) Full FTIR spectra of indomethacin and titania powders. The blue box indicates the region accessible with the QCL. This region of the spectra is zoomed in and shown in part d overlaid with the AF-PTIR spectra of both components. QCL spectral channels used for on- and off-resonance image acquisitions are shown with green vertical lines. (b,c) AF-PTIR image of pure indomethacin powder acquired with 1085 $cm^{-1}$ (on-resonance) and 1122 $cm^{-1}$ (off-resonance) QCL channels, respectively, plotted at the same scale. (e,f) AF-PTIR images of pure titania powder acquired at the same spectral channels.

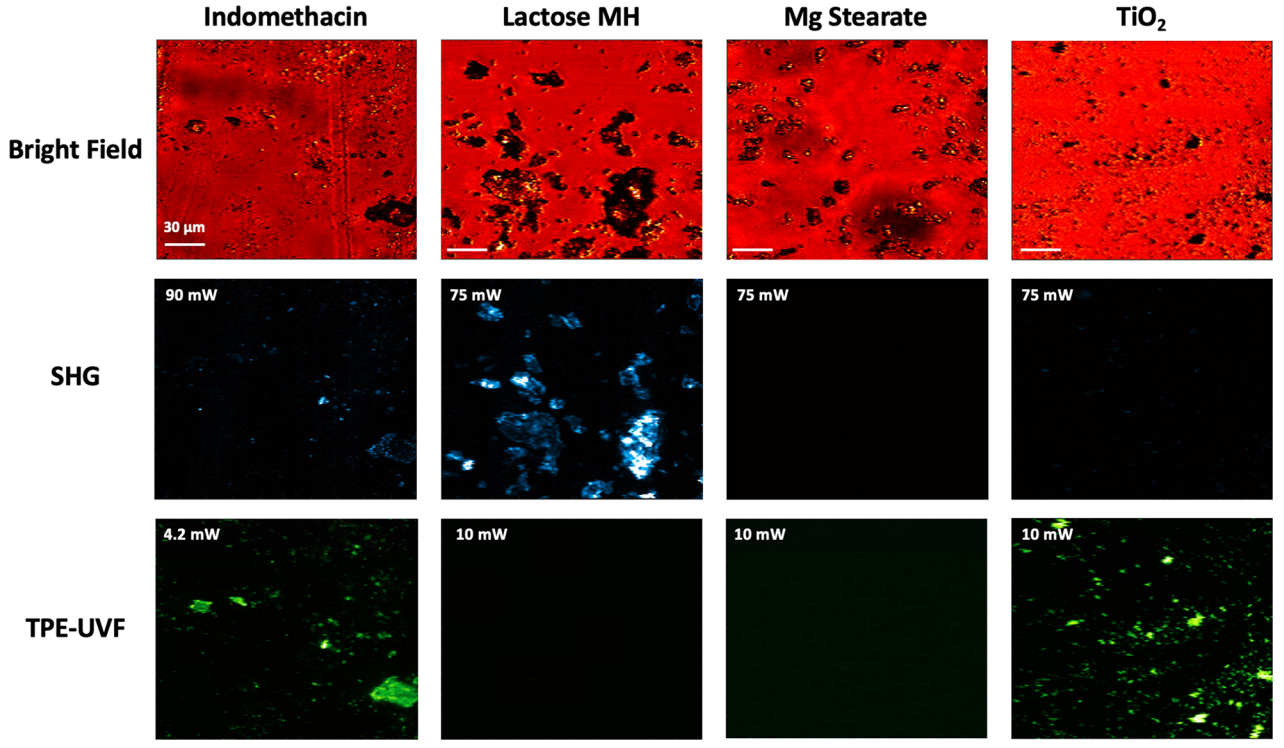


**Figure 3.** Bright field, SHG, and TPE-UVF images of individual component crystalline powders. All images collected with one method are presented at the same brightness scale. Bright field was collected by measuring the transmitted light. SHG and TPE-UVF were collected in an epi-configuration with incident wavelengths of 532 and 1064 nm, respectively, by switching the filter sets in front of the detector. Incident radiation power was measured right before the sample plane.

(Figure 1c). A spatial resolution for TPE-UVF image was calculated to be 0.79 $\mu$m by edge derivative analysis, which is slightly less than the 0.54 $\mu$m theoretical maximum predicted for Gaussian optics.



https://doi.org/10.1021/acs.analchem.1c05504
Anal. Chem. 2022, 94, 6512−6520

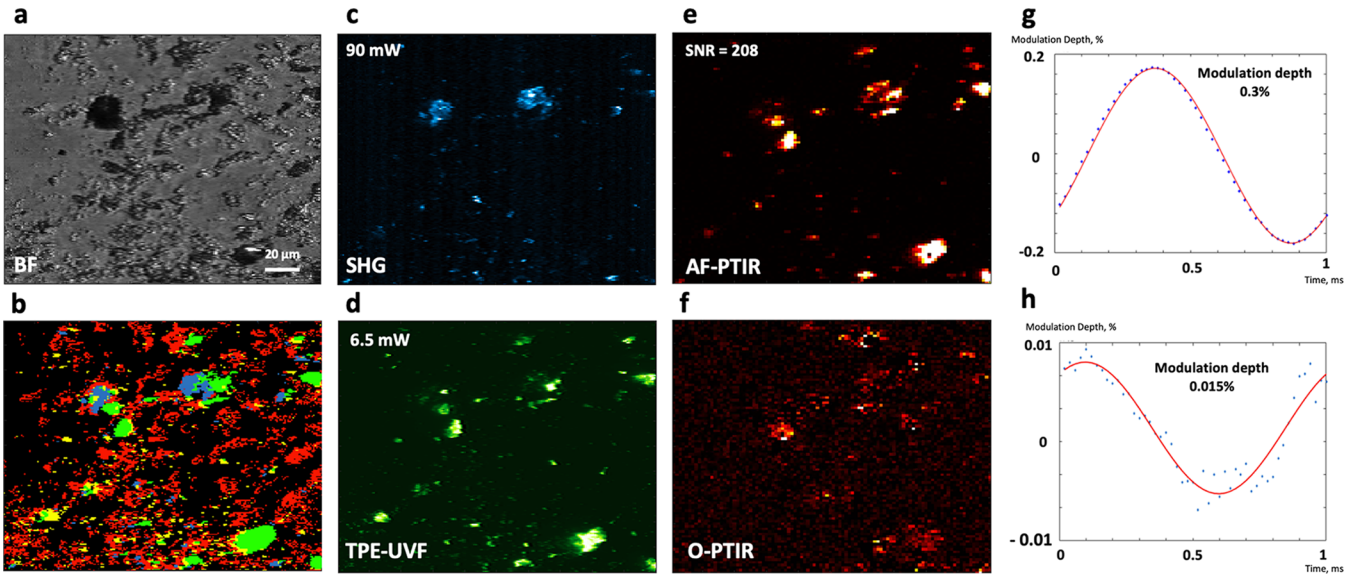


**Figure 4.** Photothermal and nonlinear optical microscopy of a multicomponent mixture. (a,c–f) Bright field, SHG, TPE-UVF, AF-PTIR, and O-PTIR images of the field of view, respectively. All images were collected using the AF-PTIR multimodal instrument. (b) Segmentation results showing the spatial distribution of individual components (lactose particles are shown in blue, indomethacin in green, $TiO_2$ in yellow, and Mg stearate is shown in red). (g,h) Single pixel signal intensity averaged over the QCL modulation period and corresponding modulation depth for AF-PTIR and O-PTIR (calculated relative to backscattered light intensity) images, respectively.

The mid-IR spectrum of indomethacin in the fingerprint region was recovered by measuring the AF-PTIR intensity when cycling through each of the individual QCL channels. The TPE-UVF photothermal spectrum shown in Figure 2d was acquired by averaging across the bright regions in the field of view. The spectrum agrees well with ATR-FTIR spectra of pure indomethacin powders. The notable deviation of the peak around 1060 $cm^{-1}$ from its center position in FTIR spectrum is tentatively attributed to differences in signal-to-noise in the spectral measurements. The lowest energy spectral channels also exhibited the lowest power outputs (see the Supporting Information), which correlated with greater disparities between the FTIR and F-PTIR spectra.

The relative intensity of the AF-PTIR signal for on- and off-resonance cases is compared in Figure 2b,c, indicating correlations between AF-PTIR brightness and mid-IR absorption. The AF-PTIR signal intensity at the same spectral channels was also compared for titanium dioxide powder. $TiO_2$ is a common pharmaceutical excipient exhibiting substantial TPE-UVF activity (Figure 1c). AF-PTIR images of pure $TiO_2$ powder were collected for the same two channels as used for indomethacin, shown in Figure 2e,f. No substantial difference in AF-PTIR intensity was observed for these two spectral channels for $TiO_2$, in contrast to the indomethacin response.

**Nonlinear Optical Microscopy of Indomethacin and Pharmaceutical Excipients.** Complementary measurements were performed on pure materials and on prepared mixtures of materials designed to reflect the contents of commercially available final dosage forms of indomethacin.[40] Indomethacin capsules contain a mixture of indomethacin, $\alpha$-lactose monohydrate, sodium lauryl sulfate, sodium starch glycolate, magnesium stearate, titanium dioxide, and colloidal silicon dioxide encapsulated within a hard shell made of gelatin and coloring agents. Four materials were investigated to represent the major classes of materials used, including the API itself, lactose monohydrate (often added for tableting), magnesium stearate as a representative surfactant, and $TiO_2$ as a representative inorganic constituent (often added to tablets as a pigment or to minimize UV exposure). Bright field, SHG, and TPE-UVF images of these four isolated representative materials are shown in Figure 3.

The observations for the pure components shown in Figure 3 are in good agreement with both chemical intuition and prior published work.[34,41] Pure indomethacin showed the strongest TPE-UVF activity among the tested compounds. However, titania microparticles produced a similarly bright image under slightly over than twice of the laser power used to image the API crystals. Lactose crystals showed the strongest SHG activity consistent with the noncentrosymmetry inherent in the lactose MH lattice. Magnesium stearate was the only compound that was found to be inactive for both SHG and two-photon fluorescence, visualized by using laser transmittance alone.

**Quantitative Capabilities.** The AF-PTIR results were used to obtain quantitative estimates of the sensitivity and the limit of detection of the method. The volume fraction of AF-PTIR active particles within a field of view (FoV) assuming spherical particles was found to be ~25%. Following the method of Smith et al.[42] for autocalibration in image analysis, the value of integrated AF-PTIR intensity per unit volume was 190 counts/$\mu m^3$. Based on the noise floor level measured in the absence of QCL modulation, we estimate that the smallest particle that can be detected using AF-PTIR with SNR $\geq$ 3 corresponds to a limit of detection of 0.16 $\mu m^3$ or 5 ppm. This LoD corresponds to detection of a single particle of 0.67 $\mu$m diameter in a 200 × 200 $\mu m^2$ FoV.

The absolute sensitivity of AF-PTIR measurements was assessed by estimation of the total photon count. An average integrated voltage over a 100 ns window for our instrument was 0.327 mV/photon. During the measurement, the measured voltage over the same 100 ns window was 15.65 mV, which corresponds to roughly 48 photons per 100 ns or $4.8 \times 10^8$ photons per second. Based on Poisson statistics, a modulation depth of 1% is expected to enable measurements


https://doi.org/10.1021/acs.analchem.1c05504
Anal. Chem. 2022, 94, 6512–6520

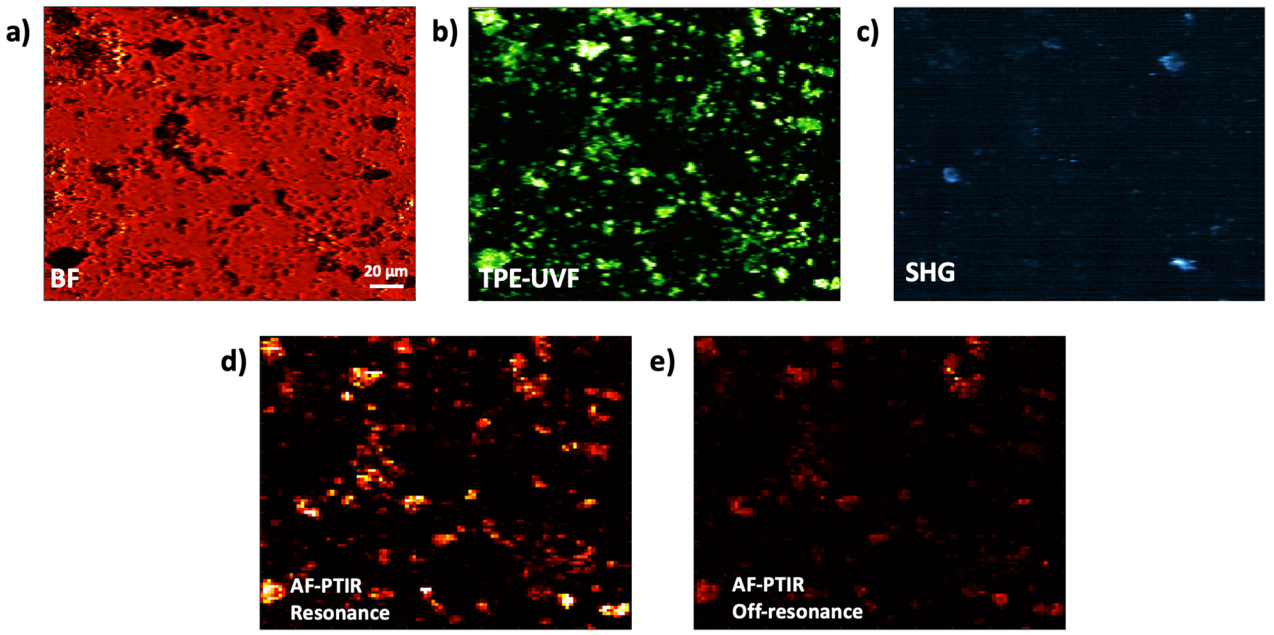


**Figure 5.** Photothermal and nonlinear optical microscopy of a commercial indomethacin capsule. (a−c) Bright field, TPE-UVF, and SHG images of the used FoV, respectively. (d,e) On- and off-resonance AF-PTIR images collected using the same QCL sequences that were used in Figure 4.

with the SNR around 40 for a 30 ms pixel dwell time [$1.4 \times 10^5$photons/$\sqrt{1.4 \times 10^7}$photons]. In practice, the observed SNR exceeded this Poisson metric at several locations, suggesting modulation depths of several percent during the acquisition.

**AF-PTIR Mapping of the Drug Distribution and Identification of Excipients with Multimodal Nonlinear Optical Microscopy.** A physical mixture of four representative components was prepared to test the capabilities and limitations of nonlinear optical microscopy for pharmaceutical substances imaging and analysis. The results of bright field, SHG and TPE-UVF measurements are demonstrated in Figure 4a,c,d. As expected for multimodal imaging, contrast for different species varied qualitatively across the different measurement suites.

AF-PTIR microscopy was applied to perform vibrational analysis of the TPE-UVF active domains, which potentially include both indomethacin and titanium dioxide. The image in Figure 4e was produced while serially activating 5 QCL channels that correspond to the strongest mid-IR absorption of indomethacin based on its IR spectrum (1069, 1081, 1085, 1089, and 1149 $cm^{-1}$) and absence of significant titania absorption at those same wavelengths (Figure 2a). Analogous measurements acquired with IR channels that exhibit weak indomethacin absorption (1054, 1058, 1158, 1162, and 1167 $cm^{-1}$) yielded notable reductions in AF-PTIR response (Supporting Information). The high spectral sensitivity of AF-PTIR to wavelengths corresponding to peaks in indomethacin absorption support assignment of the particles in Figure 4 to indomethacin.

For comparison with AF-PTIR, conventional O-PTIR microscopy measurements based on absorption-induced perturbation to visible light scattering was performed, the results of which are summarized in Figure 4f. As in AF-PTIR, the O-PTIR image was acquired with the QCL was tuned to match the indomethacin absorption maxima, shown in Figure 4f. Additionally, O-PTIR images collected while operating QCL sequences optimized for lactose and Mg stearate absorption are provided in the Supporting Information. The modulation depth was calculated for the brightest pixel in each of the AF-PTIR and O-PTIR images (Figure 4g,h). While in principle, O-PTIR has the advantage of not requiring UV fluorescence, the selectivity to indomethacin and signal-to-noise are reduced relative to AF-PTIR. However, it should be noted that the O-PTIR measurements were performed using home-built instrumentation; fully optimized commercial instrumentation may yield improvements in SNR relative to that shown in Figure 4f. Nevertheless, these trends are consistent with enhancements in SNR for F-PTIR relative to O-PTIR reported by Cheng and co-workers.[27] Based on the fitting uncertainties for the recovered modulation amplitudes in Figure 4g,h, fluorescence-based photothermal microscopy resulted in a 7.8-fold difference for the depth of modulation.

Collectively, TPE-UVF and SHG imaging of the mixture supported by AF-PTIR microscopy can be applied to map the distribution of individual components within a field of view. The threshold-based segmentation process for particle identification using bright field images as shown in Figure 4a is described in the Supporting Information, and the resulting segmented and classified image is demonstrated in Figure 4b, in which each individual component is shown in a different color. Most of the smaller particles found within the studied FoV did not produce detectable TPE-UVF or SHG and were classified as Mg stearate particles. As a caveat, small particles producing signals below the limits of detection for SHG or TPE-UVF will by default classify as magnesium stearate and may be prone to misclassification. Limits of detection for both methods are estimated be on the order of parts per million, corresponding to detection of single ∼1−5 $\mu$m crystals in ∼2 mm by 2 mm fields of view.[43] Particles that were bright for SHG but inactive for TPE-UVF measurements were classified as lactose monohydrate. Titania and indomethacin are both TPE-UVF active based on the results shown in Figure 3. However, AF-PTIR microscopy enabled assignment of the TPE-UVF particles to the indomethacin crystals based on the


https://doi.org/10.1021/acs.analchem.1c05504
Anal. Chem. 2022, 94, 6512−6520

differences in IR absorption between the two particle classes shown in Figure 2.

## DISCUSSION

The integration of AF-PTIR with multimodal imaging improves confidence in chemical classification for analysis of powdered mixtures. As demonstrated for pure constituents' powders in Figure 3, titania microparticles can produce clearly detectable TPE-UVF signals, such that the presence of TPE-UVF alone cannot unambiguously be used to assign indomethacin particles. The indomethacin sample used was comprised of the centrosymmetric $\gamma$-form (space group $P\bar{1}$), with the relatively weak signal on the SHG channel tentatively attributed to break-through of visible-wavelength two photon excited fluorescence. While the $\alpha$-form of indomethacin is noncentrosymmetric and can support bulk-allowed coherent SHG, powder X-ray diffraction measurements confirmed the dominance of the $\gamma$-polymorph (Supporting Information). Furthermore, changes in the filter set for optimization of two-photon excited fluorescence with 1064 nm excitation (described in the Supporting Information) yielded contrast similar to that detected on the SHG channel. The spurious apparent SHG signals from indomethacin have the potential to complicate definitive assignment of lactose microcrystals. Both ambiguities from TPE-UVF and SHG as stand-alone methods were effectively addressed through IR absorption spectroscopy of individual microparticles by AF-PTIR.

Complementary measurements on a commercial indomethacin final dosage form suggest that the capsule contents were comprised of isolated particles of a size distribution similar to that of our model preparation, with both SHG and TPE-UVF observed from the sample (Figure 5). AF-PTIR measurements of the TPE-UVF active particles were spectroscopically consistent with those recorded for pure indomethacin and were assigned as such. The commercial capsule had a significantly higher volume fraction of indomethacin compared to the mixture shown in Figure 4.

It should be clear that AF-PTIR is exclusively limited to APIs exhibiting sufficient TPE-UVF to support fluorescence-based analysis as a complement to O-PTIR. The results shown in Figure 1c are an expansion of results originally compiled by Toth and co-workers.[34] The highlighted upper region of the plot indicates the moieties producing TPE-UVF well above the noise floor of the instrument and therefore potentially amenable to AF-PTIR analysis. From this admittedly small survey of pharmaceutical materials, 46% of small molecule APIs produce detectable TPE-UVF and could potentially contribute to an AF-PTIR response. In contrast, HPMC was the only excipient producing substantial TPE-UVF activity. However, it is worth noting that activities are plotted on log-scales; species exhibiting relatively weak TPE-UVF responses may require significantly longer integration times for comparable signal-to-noise in detection. Using ritonavir as a benchmark for which TPE-UVF measurements are clearly observable,[26] ~50% of the APIs exhibit TPE-UVF activity potentially bright enough to support AF-PTIR.

Additionally, AF-PTIR microscopy suggests several practical advantages complementing stand-alone measurements by O-PTIR imaging. First, due to the significantly higher temperature-induced variations, fluorescence intensity is a more sensitive signal reporter compared to refractive index change, consistent with the increased signal-to-noise in the AF-PTIR images. Furthermore, AF-PTIR enables selective vibrational spectroscopy with higher intrinsic selectivity to the API-rich regions of primary interest when characterizing drug distributions within dosage forms. In the studied case, API particles were mixed at a relatively small volume fraction but imaged with negligible interference from TPE-UVF inactive excipients by AF-PTIR. O-PTIR produced broad applicability across all analytes but with lower sensitivity to indomethacin. For the mixture discussed here, lactose and indomethacin exhibited higher absorption cross sections relative to other components in the mixture, which resulted in significant cross-talk in demultiplexed O-PTIR images designed to optimally discriminate based on mid-IR absorption at the accessible QCL wavelength channels (details are provided in the Supporting Information).

AF-PTIR imaging complements targeted spectroscopy of locations adjacent to site-specific fluorescence labels in F-PTIR. In prior studies with F-PTIR, fluorescence labeling enabled highly localized chemical characterization of cell organelles and single bacteria, supporting measurements of the composition of regions adjacent to selective structures of interest.[26,27] The present studies by AF-PTIR provide complementary label-free analysis adjacent to aromatic moieties that can, in principle, be acquired concurrently with targeted F-PTIR (e.g., through simultaneous one and two photon excited fluorescence). Pairing of multiple complementary imaging modalities, such as AF-PTIR, F-PTIR, O-PTIR, with independent contrast methods such as SHG can significantly improve the classification confidence, as demonstrated in Figure 4.

Given that the infrared excitation is within the same molecule as the electronic transition driving fluorescence, it is worthwhile to consider contributions to the AF-PTIR signal from coherent intramolecular interactions, such as resonance-enhanced three photon excitation (IR + vis + vis). The peak power of the mid-IR QCL source was $\sim 10^{-9}$ of the peak power of the excitation beam, when accounting for the significantly lower power and ~15 times larger focal spot-size of the former. As such, for every 1 IR photon overlapping with a given visible pulse, $10^9$ mid-IR photons not spatially or temporally coincident were contributing to the AF-PTIR response. Given both the low spatiotemporal overlap combined with the overall inefficiency of three-photon absorption compared to two-photon excitation, three-photon processes were assumed to contribute negligibly to the detected AF-PTIR signal.

It should be noted that because AF-PTIR relies on fluorescence emission as the signal generation source, effects such as self-quenching in crystals might potentially impact the total fluorescence signal. As was demonstrated previously,[26] self-quenching could influence the relative autofluorescence brightness of molecular crystals with different polymorphs. Autoquenching generally competes with fluorescence, such that transient temperature changes may significantly affect the balance between fluorescence and autoquenching. The total AF-PTIR signal scales with the combined product of the quantum efficiency and the derivative of the QE with temperature. As such, it is not immediately obvious how self-quenching will impact the sensitivity of AF-PTIR (decreases in QE may be offset by increases in $dQE/dT$). Additional AF-PTIR studies performed on different polymorphic forms of otherwise identical crystals may help disentangle these competing effects. In any case, autoquenching can be reasonably expected to be independent of the IR wavelength


https://doi.org/10.1021/acs.analchem.1c05504
Anal. Chem. 2022, 94, 6512−6520

responsible local absorption and heating, such that classification based on AF-PTIR vibrational spectral analysis should not be substantially affected by overall differences in absolute quantum efficiency.

The ubiquity of TPE-UVF active aromatic groups natively present within many samples of interest suggest broad applicability of AF-PTIR in studies of biologically relevant materials. The present study suggests utility for label-free analysis of many pharmaceutical materials with high selectivity for the API, complementing previous O-PTIR measurements by Li et al.[24] The extensive use of TPE-UVF for native protein imaging[44,45] suggests applications for studying lyophilized and crystalline protein particles and tissue sections. Multiphoton excited autofluorescence of NADH is commonly used to probe local cell metabolism and could provide yet another complementary local label-free probe for AF-PTIR analysis.[46,47]

## CONCLUSION

Autofluorescence-detected photothermal mid-IR (AF-PTIR) microscopy was demonstrated as a label-free technique and applied to map the spatial distribution of indomethacin in a mixture containing representative pharmaceutical excipients. AF-PTIR microscopy provided an additional level of selectivity for nonlinear optical imaging of pharmaceutical final dosage forms through mid-IR spectroscopy with high spatial resolution. When combined with bright field, SHG, and TPE-UVF imaging, AF-PTIR enabled segmentation of the field-of-view to visualize each of the individual mixture components. AF-PTIR achieved improved chemical selectivity and signal-to-noise characteristics when compared to optically detected photothermal microscopy for pharmaceutical materials analysis. AF-PTIR has the potential to aid in assessing content uniformity in pharmaceutical tablets production by rapidly visualizing the spatial distribution of active pharmaceutical ingredients within final dosage forms. It is also interesting to consider possible future applications of AF-PTIR for analysis of therapeutic macromolecular formulations of protein-based biologics. Previous demonstration of TPE-UVF in proteins[48] along with preliminary proof-of-concept AF-PTIR measurements of tryptophan microcrystals and lyophilized protein particles[26] suggests potential compatibility with biologics formulations analysis.

## ASSOCIATED CONTENT

### Supporting Information

The Supporting Information is available free of charge at https://pubs.acs.org/doi/10.1021/acs.analchem.1c05504.

Additional information is provided describing: (i) IR spectra of individual components and QCL specifications, (ii) image segmentation details, (iii) PXRD results, (iv) additional O-PTIR measurements, (v) indomethacin visible fluorescence measurements, (vi) legend for Figure 1c, and (vii) SNR map for AF-PTIR measurements (PDF)

## AUTHOR INFORMATION


### Corresponding Author

**Garth J. Simpson** − *Department of Chemistry, Purdue University, West Lafayette, Indiana 47907, United States;* orcid.org/0000-0002-3932-848X; Email: gsimpson@purdue.edu

### Authors

**Aleksandr Razumtcev** − *Department of Chemistry, Purdue University, West Lafayette, Indiana 47907, United States;* orcid.org/0000-0001-9591-8612

**Minghe Li** − *Department of Chemistry, Purdue University, West Lafayette, Indiana 47907, United States*

**Jiayue Rong** − *Department of Chemistry, Purdue University, West Lafayette, Indiana 47907, United States*

**Chu C. Teng** − *Pendar Technologies, Cambridge, Massachusetts 02138, United States*

**Christian Pfluegl** − *Pendar Technologies, Cambridge, Massachusetts 02138, United States*

**Lynne S. Taylor** − *Physical and Industrial Pharmacy, Purdue University, West Lafayette, Indiana 47907, United States;* orcid.org/0000-0002-4568-6021

Complete contact information is available at: https://pubs.acs.org/10.1021/acs.analchem.1c05504


### Author Contributions

‖A.R. and M.L. contributed equally. A.R. and M.L. performed the experiments and data analysis. J.R. assisted with the instrument design. C.C.T. and C.P. developed and characterized the QCL array. L.S.T. and G.J.S. managed and supervised the project.

### Notes

The authors declare the following competing financial interest(s): C.C.T. and C.P. work at a company "Pendar Technologies" that incorporates the QCL into commercial products.

## ACKNOWLEDGMENTS

M.L., A.R., and G.J.S. gratefully acknowledge funding from the National Science Foundation (Grants GOALI-CHE-1710475, NSF-D3SC-2004046, and CIF-1763896). M.L. and A.R. also acknowledge support from the NSF Center for Bioanalytic Metrology (Grant IIP-1916691). A.R. also acknowledges the Purdue Research Foundation for a Graduate Scholarship. Pendar Technologies acknowledges support from the U.S. Army under SBIR topic A14A-T015.

## REFERENCES


(1) Kanfer, I.; Walker, R.; Löbenberg, R.; Bou-Chacra, N. *Experimental Formulation Development* **2013**, *20133059*, 51−94.

(2) Rohrs, B. R.; Amidon, G. E.; Meury, R. H.; Secreast, P. J.; King, H. M.; Skoug, C. J. *J. Pharm. Sci.* **2006**, *95* (5), 1049−1059.

(3) Cruz, J.; Blanco, M. *J. Pharm. Biomed. Anal.* **2011**, *56* (2), 408−412.

(4) Spengler, B. *Anal. Chem.* **2015**, *87* (1), 64−82.

(5) Kettling, H.; Vens-Cappell, S.; Soltwisch, J.; Pirkl, A.; Haier, J.; Müthing, J.; Dreisewerd, K. *Anal. Chem.* **2014**, *86* (15), 7798−7805.

(6) Kompauer, M.; Heiles, S.; Spengler, B. *Nat. Methods* **2017**, *14* (1), 90−96.

(7) Liébana-Martos, C. *Indications, Interpretation of Results, Advantages, Disadvantages, and Limitations of MALDI-TOF*; Elsevier Inc., 2018; DOI: 10.1016/B978-0-12-814451-0.00005-8.

(8) Bergman, N.; Shevchenko, D.; Bergquist, J. *Anal. Bioanal. Chem.* **2014**, *406* (1), 49−61.

(9) Davis, B. J.; Carney, P. S.; Bhargava, R. *Analytical chemistry* **2010**, *82* (9), 3474−3486.

(10) Reddy, R. K.; Walsh, M. J.; Schulmerich, M. V.; Carney, P. S.; Bhargava, R. *Appl. Spectrosc.* **2013**, *67* (1), 93−105.

(11) Zhang, Y.; Johnson, K. C. *Int. J. Pharm.* **1997**, *154* (2), 179−183.

(12) Kuriyama, A.; Ozaki, Y. *AAPS PharmSciTech* **2014**, *15* (2), 375−387.
(13) Smith, G. P. S.; McGoverin, C. M.; Fraser, S. J.; Gordon, K. C. *Adv. Drug Delivery Rev.* **2015**, *89*, 21−41.
(14) Zhu, X.; Xu, T.; Lin, Q.; Duan, Y. *Appl. Spectrosc. Rev.* **2014**, *49* (1), 64−82.
(15) El-Diasty, F. *Vib. Spectrosc.* **2011**, *55* (1), 1−37.
(16) Tu, H.; Boppart, S. A. *Journal of biophotonics* **2014**, *7* (1−2), 9−22.
(17) Dazzi, A.; Prazeres, R.; Glotin, F.; Ortega, J. M. *Opt. Lett.* **2005**, *30* (18), 2388.
(18) Dazzi, A.; Prater, C. B. *Chem. Rev.* **2017**, *117* (7), 5146−5173.
(19) Dazzi, A.; Glotin, F.; Carminati, R. *J. Appl. Phys.* **2010**, *107* (12), 124519.
(20) Zhang, D.; Li, C.; Zhang, C.; Slipchenko, M. N.; Eakins, G.; Cheng, J.-X. *Science Advances* **2016**, *2* (9), e1600521.
(21) Lee, E. S.; Lee, J. Y. *Opt. Express* **2011**, *19* (2), 1378.
(22) Zhang, Y.; Yurdakul, C.; Devaux, A. J.; Wang, L.; Xu, X. G.; Connor, J. H.; Ünlü, M. S.; Cheng, J.-X. *Anal. Chem.* **2021**, *93* (8), 4100−4107.
(23) Pavlovetc, I. M.; Podshivaylov, E. A.; Chatterjee, R.; Hartland, G. V.; Frantsuzov, P. A.; Kuno, M. *J. Appl. Phys.* **2020**, *127* (16), 165101.
(24) Li, C.; Zhang, D.; Slipchenko, M. N.; Cheng, J. X. *Anal. Chem.* **2017**, *89* (9), 4863−4867.
(25) Tokeshi, M.; Uchida, M.; Hibara, A.; Sawada, T.; Kitamori, T. *Anal. Chem.* **2001**, *73* (9), 2112−2116.
(26) Li, M.; Razumtcev, A.; Yang, R.; Liu, Y.; Rong, J.; Geiger, A. C.; Blanchard, R.; Pfluegl, C.; Taylor, L. S.; Simpson, G. J. *J. Am. Chem. Soc.* **2021**, *143* (29), 10809−10815.
(27) Zhang, Y.; Zong, H.; Zong, C.; Tan, Y.; Zhang, M.; Zhan, Y.; Cheng, J.-X. *J. Am. Chem. Soc.* **2021**, *143* (30), 11490−11499.
(28) Clydesdale, G.; Hammond, R. B.; Roberts, K. J. *J. Phys. Chem. B* **2003**, *107* (20), 4826−4833.
(29) Land, T. A.; Martin, T. L.; Potapenko, S.; Palmore, G. T.; de Yoreo, J. J. *Nature* **1999**, *399* (6735), 442−445.
(30) Brestrich, N.; Rudt, M.; Buchler, D.; Hubbuch, J. *Chem. Eng. Sci.* **2018**, *176*, 157−164.
(31) Bushey, M. M.; Jorgenson, J. W. *Anal. Chem.* **1990**, *62* (10), 978−984.
(32) Li, Q.; Seeger, S. *Appl. Spectrosc. Rev.* **2010**, *45* (1), 12−43.
(33) Toth, S. J.; Schmitt, P. D.; Snyder, G. R.; Trasi, N. S.; Sullivan, S. Z.; George, I. A.; Taylor, L. S.; Simpson, G. J. *Cryst. Growth Des.* **2015**, *15* (2), 581−586.
(34) Toth, S. J.; Madden, J. T.; Taylor, L. S.; Marsac, P.; Simpson, G. J. *Anal. Chem.* **2012**, *84* (14), 5869−5875.
(35) Isobe, K.; Takeda, T.; Mochizuki, K.; Song, Q.; Suda, A.; Kannari, F.; Kawano, H.; Kumagai, A.; Miyawaki, A.; Midorikawa, K. *Biomedical Optics Express* **2013**, *4* (11), 2396.
(36) Chen, W.; Xiong, Y.; Wang, W.; Wu, T.; Li, L.; Kang, Q.; Du, Y. *Talanta* **2019**, *203*, 77−82.
(37) Cao, L.; Wang, X.; Meziani, M. J.; Lu, F.; Wang, H.; Luo, P. G.; Lin, Y.; Harruff, B. A.; Veca, L. M.; Murray, D.; Xie, S.-Y.; Sun, Y.-P. *J. Am. Chem. Soc.* **2007**, *129* (37), 11318−11319.
(38) Haupert, L. M.; Simpson, G. J.; Slipchenko, L. v. *J. Phys. Chem. A* **2011**, *115* (36), 10159−10165.
(39) Fennelly, M. J.; Sewell, G.; Prentice, M. B.; O'Connor, D. J.; Sodeau, J. R. *Atmosphere* **2018**, *9*, 1.
(40) National Center for Biotechnology Information. *PubChem Annotation Record for INDOMETHACIN, Source: Hazardous Substances Data Bank (HSDB)*, https://pubchem.ncbi.nlm.nih.gov/source/hsdb/3101.
(41) Rawle, C. B.; Lee, C. J.; Strachan, C. J.; Payne, K.; Manson, P. J.; Rades, T. *J. Pharm. Sci.* **2006**, *95* (4), 761−768.
(42) Smith, C. J.; Dinh, J.; Schmitt, P. D.; Stroud, P. A.; Hinds, J.; Johnson, M. J.; Simpson, G. J. *Appl. Spectrosc.* **2018**, *72* (11), 1594−1605.
(43) Chowdhury, A. U.; Zhang, S.; Simpson, G. J. *Anal. Chem.* **2016**, *88* (7), 3853−3863.
(44) Madden, J. T.; DeWalt, E. L.; Simpson, G. J. *Acta Crystallogr.* **2011**, *D67*, 839−846.
(45) Kestur, U. S.; Wanapun, D.; Toth, S. J.; Wegiel, L. A.; Simpson, G. J.; Taylor, L. S. *Journal of pharmaceutical sciences* **2012**, *101* (11), 4201−4213.
(46) Chance, B.; Cohen, P.; Jobsis, F.; Schoener, B. *Science* **1962**, *137* (3529), 499−508.
(47) Vergen, J.; Hecht, C.; Zholudeva, L. v; Marquardt, M. M.; Hallworth, R.; Nichols, M. G. *Microscopy and Microanalysis* **2012**, *18* (4), 761−770.
(48) Kissick, D. J.; Gualtieri, E. J.; Simpson, G. J.; Cherezov, V. *Anal. Chem.* **2010**, *82* (2), 491−497.




https://doi.org/10.1021/acs.analchem.1c05504
*Anal. Chem.* 2022, 94, 6512−6520